Sedimentary Geology 466 (2024) 106649

Contents lists available at ScienceDirect

Sedimentary Geology

journal homepage: www.elsevier.com/locate/sedgeo

# The source and preservation of lacustrine shale organic matter: Insights from the Qingshankou Formation in the Changling Sag, Southern Songliao Basin, China

Lei Li [a,b,c], Zhidong Bao [a,b,*], Long Li [c], Zhongcheng Li [d], Shuyue Ban [a], Zongfeng Li [a], Tengyu Wang [a], Yilin Li [a], Naixi Zheng [a], Chenxu Zhao [d], Li Chen [d], Jianwen Chen [d]

[a] College of Geosciences, China University of Petroleum-Beijing, Beijing 102249, China
[b] State Key Laboratory of Petroleum Resource and Prospecting, China University of Petroleum-Beijing, Beijing 102249, China
[c] Department of Earth and Atmospheric Sciences, University of Alberta, Edmonton, Alberta, Canada
[d] Research Institute of Exploration and Development, PetroChina Jilin Oilfield Company, Jilin 138000, China

ARTICLE INFO

*Article history:*
Received 4 March 2024
Received in revised form 10 April 2024
Accepted 14 April 2024
Available online 19 April 2024

Editor: Dr. Massimo Moretti

*Keywords:*
Shale organic matter
Source-preservation
Sedimentary environment
Clay minerals
Qingshankou Formation
Songliao Basin

ABSTRACT

Organic-rich shale in the Cretaceous succession of the large non-marine Songliao Basin in northeastern China, especially the Qingshankou Formation of the Turonian and Coniacian stages, provides a unique record for studying the role of global climate control on organic matter accumulation. Organic enrichment in the Qingshankou Formation along the Southeastern Uplift of the basin has been widely reported and is implicated in the formation of algal blooming and a saline anoxic water environment. However, studies on the Qingshankou Formation in the Changling Sag are relatively few, which leaves a significant gap to understand the controlling factors of organic enrichment at a basin scale. In this study, the sedimentary environment of the first member of the Upper Cretaceous Qingshankou Formation ($K_2qn^1$) is reconstructed from petrological and geochemical data to discuss the sources and preservation mechanisms of lacustrine shale organic matter in the Changling Sag (southern Songliao Basin). The $K_2qn^1$ is subdivided into three stratigraphic units: Sq1 phase, Sq2 phase, and Sq3 phase. Biomarker (abundance of tricyclic terpane and regular steranes) and petrographical (maceral composition) data indicate that the organic matter in $K_2qn^1$ was mainly from terrigenous plants, with some algal input. Inorganic minerals (major and trace elements) and petrological (framboidal pyrite size) data suggest a humid climate and saline anoxic water environment at the Changling Sag during the most organic-rich Sq1 phase. During the Sq2 and Sq3 phases, a relative low lake level and semi-arid climatic conditions likely prevailed. Moreover, these results imply that apart from a saline anoxic water environment, the persistence of continentally derived organic matter in lacustrine shale is mainly controlled by clay minerals. Accordingly, this study proposed a new enrichment model for lacustrine shale organic matter. The new model complements existing lacustrine shale sedimentary models for sources of organic matter and emphasizes the role of clay minerals in preserving organic matter.



## 1. Introduction

The factors affecting organic matter enrichment include climatic fluctuations and corresponding hydrodynamic conditions, source mixing and organic matter flocculation (Neumeister et al., 2020; Khaled et al., 2022). For example, a sedimentary environment similar to the modern Black Sea, characterized by high salinity, anoxia, and the predominance of organic-rich black mud, facilitates the formation of organic-rich shales. Accordingly, a "Black Sea Mud" sediment model has been proposed (Tourtelot, 1979). However, shale can form not only in marine environments, but more broadly in transitional, and terrestrial sedimentary environments (Tourtelot, 1979; Zou et al., 2013; Wu et al., 2021). The "Black Sea Mud" model cannot explain the origin of organic-rich shale in continental facies. Subsequently, additional sedimentary models have been proposed for organic-rich black shales (Zou et al., 2013). These models share similarities in sedimentary mechanisms, which involve (i) rapid lake-level rise (due to Earth's dynamic processes, including climate change) that created extensive anoxic conditions in the deep water and drove the oxygen minimum zone toward shallow water, (ii) consequent enhanced productivity in shallow water led to an excess supply of organic matter and excessive oxygen consumption, and (iii) as a result, the intermittent surface water anoxia, accelerating organic matter settling, burial,

* Corresponding author at: College of Geosciences, China University of Petroleum-Beijing, Beijing 102249, China.
*E-mail address:* baozhd@cup.edu.cn (Z. Bao).

https://doi.org/10.1016/j.sedgeo.2024.106649
0037-0738/

and preservation ultimately helped to form organic-rich shales. However, these sedimentary models do not address organic deposition and preservation (especially the unique role of clay minerals) in the context of paleoenvironmental changes.

The Cretaceous was characterized by greenhouse climate in geological history, including a series of significant geological events, which occurred at the Cenomanian–Turonian boundary, such as the Oceanic Anoxic Event 2 (Sageman et al., 2006), high sea levels (Jenkyns, 2010), the absence of sustained ice sheets (MacLeod et al., 2013), and the formation of large igneous provinces (Scaife et al., 2017). These have led to global development of organic-rich shale in this specific period in the Cretaceous (Owens et al., 2018). In recent years, the formation environment of organic-rich shale in the Western Tethys, original North Atlantic, and South Atlantic shallow sea areas has been examined in detail (Demaison and Moore, 1980; Kuypers et al., 2001; Schouten et al., 2003), which provide an important reference for exploring the relationship between global environmental change and deposition of organic matter. However, most of these climate change records have been obtained from marine sediments (Hasegawa et al., 2003); there is relatively limited understanding of the terrestrial climate records, particularly in East Asia (Fig. 1a).

The Songliao Basin is the largest Mesozoic–Cenozoic continental oil and gas basin in Northeast China, with well-developed Cretaceous strata (Feng et al., 2010; Wang et al., 2013; Xi et al., 2016). Thick organic-rich shales in the Upper Cretaceous Qingshankou Formation are widely distributed and form a unique sedimentary stratum in the basin (Wang et al., 2020). In particular, shales extremely enriched in organic matter have been discovered from the first member of the Qingshankou Formation ($K_2qn^1$) in the Central Depression, confirming their great potential for shale oil and gas exploration (Zhao et al., 2020; Liu et al., 2021; Li et al., 2024). Previous studies have generally believed that the organic matter enrichment in the Qingshankou Formation is related to the formation of algal blooming and saline anoxic water environment (Feng et al., 2009, 2011). Under this context, organic accumulation is favored in muddy sediments under conditions of relatively excessive organic matter supply, relatively slow sedimentation rates, and bottom water oxidation. However, the organic matter settled in sediments can continue to undergo oxidative decomposition or be further degraded by microorganisms through processes such as fermentation, anaerobic respiration, and alkane production (Kennedy et al., 2002; Lalonde et al., 2012; Hemingway et al., 2019). Therefore, the long-term preservation mechanism of organic-rich shales is worth further exploring.

To fill this gap, we studied core samples from the Changling Sag in the southern Songliao Basin. The aims are to: (1) reconstruct the shale sedimentary environment of the $K_2qn^1$, (2) establish a sedimentary model in different sedimentary environments, and (3) propose a "source-preservation" enrichment model for organic matter.

## 2. Geological setting

The Songliao Basin, situated in the northeastern part of China, extends in a north–northeastern orientation and covers an area of approximately $26 \times 10^4$ km$^2$. It is a large composite sedimentary basin characterized by tectonic complexity (Feng et al., 2010; Zhang et al., 2018). In the Changling Sag located in the southern Songliao Basin (Fig. 1b), three stages of structural evolution are observed: rifting, sagging, and inversion. The basement is comprised of late Paleozoic to early Mesozoic metamorphic rocks and contemporaneous igneous rocks (Fig. 1c). The basin hosts primarily Cretaceous strata, reaching a maximum thickness of 7000 m (Feng et al., 2010).

During the early deposition of the Qingshankou Formation ($K_2qn$), the lake reached its maximum depth and extent, spanning an area of approximately ~$87 \times 10^3$ km$^2$ (Feng et al., 2010). In the center of this lake basin, a suite of organic-rich deep lacustrine black shales were deposited (Zhang et al., 2022) (Fig. 1d). The Qingshankou Formation is subdivided into three members ($K_2qn^1$, $K_2qn^2$, and $K_2qn^3$) based on lithology (Fig. 2).

Well A in the Changling Sag was a drilling operation specifically targeting the semi-deep to deep lake facies within the shale segments (Fig. 1d). Comprehensive analysis of core samples and well logs was conducted to identify and characterize the sequence interfaces of the $K_2qn^1$ interval in the context of land-based deepwater sedimentation and the Transgressive–Regressive cycle sequence theory (Abouelresh and Slatt, 2012). The $K_2qn^1$ interval was subdivided into three units (Sq1 phase, Sq2 phase, Sq3 phase) (Liu et al., 2019b; Zhang et al., 2022).

## 3. Material and methods

A total of 34 dark gray and gray–black shale samples representative of the main lithological units were selected from a depth range of 2360–2468 m. Each of these samples was subjected to scanning electron microscopy (SEM), X-ray diffraction (XRD), and Rock-Eval pyrolysis analyses to determine shale composition and properties. Additionally, based on the total organic carbon (TOC) distribution, 20 representative samples with TOC contents spreading over the entire range were selected for X-ray fluorescence (XRF), biomarker, and organic petrographical analyses to provide further insights into shale geochemical features.

### 3.1. Total organic carbon (TOC)

To avoid contamination, weathered or contaminated surface materials were removed from the samples by cutting. Fresh samples were then crushed and pulverized to 200-mesh powders. To remove carbonate minerals, the samples were immersed into 10 vol% hydrochloric acid (HCl) and subsequently thoroughly washed by distilled water to neutralize any remaining HCl (Ma et al., 2020). The samples were then dried in an oven at 70–80 °C. Before analysis, tungsten and iron accelerants were mixed with the sample powders. The TOC content of each sample was finally determined using a C-744 carbon analyzer.

### 3.2. Rock-Eval pyrolysis

100 mg sample powders were precisely weighed and analyzed using a Rock-Eval 6 plus pyrolysis analyzer. The samples were programmed to be heated from 300 °C (held for 3 min) to 650 °C with a heating rate of 50 °C/min. During this process, hydrocarbon abundances, including $S_1$ (volatile hydrocarbon content) and $S_2$ (remaining hydrocarbon generative potential), were quantified using a flame ionization detector. To identify the peak generation of hydrocarbons, the $T_{max}$ (calibrated temperature of maximum pyrolysis yield, °C) was carefully recorded. The hydrogen index (HI, mg HC/g TOC) was then calculated using the formula: $HI = (S2 \times 100) / TOC$ (Liu et al., 2019a).

### 3.3. XRD

The samples were first ground in an agate bowl and then sieved to select powder with a particle size of 200 mesh. For the analysis, approximately 2 to 3 g of each sample was used. The obtained powders were dried, disaggregated and then filled into aluminum sample holders. Additionally, a distinct portion of each sample was dispersed in a diluted sodium phosphate solution through the use of a sonic probe. XRD analysis was conducted using a Bruker D8 Advance goniometer (Liu et al., 2019b). The relative mineral percentage, determined by calculating the area of the main peak, was corrected for Lorentz polarization (Chalmers and Bustin, 2008).

### 3.4. Major and trace elements

Powder samples were first combusted in a muffle furnace at temperatures exceeding 1000 °C for 3–4 h (Huang et al., 2023) to calculate the loss on ignition (LOI). For the analysis of major oxides, eight doses of lithium

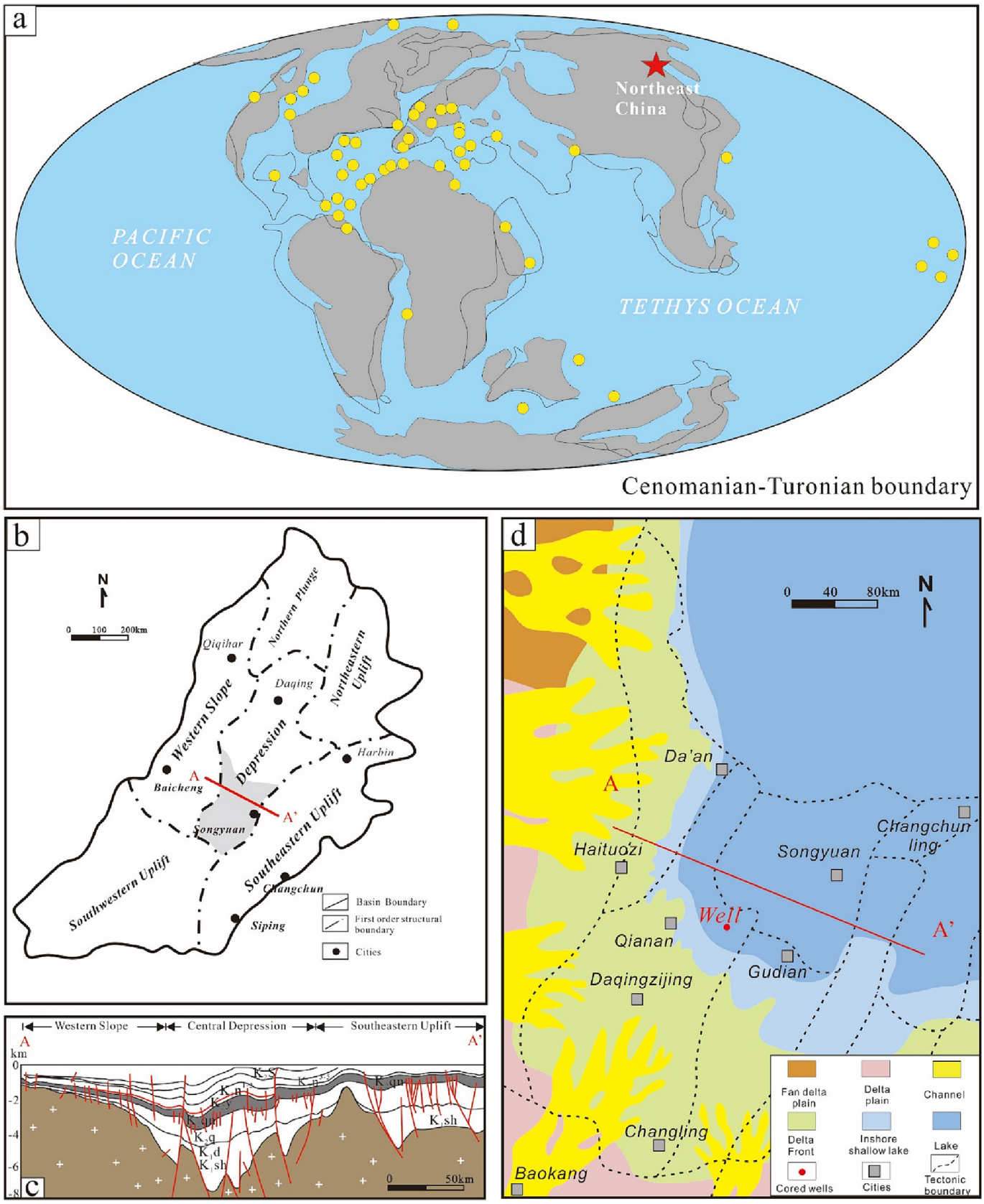


**Fig. 1.** Geological setting of the study area. (a) Locations of the OAE2 sections in the continents and drilling sites in the oceans (yellow dots) (Boulila et al., 2020); (b) structural distribution of Songliao Basin; (c) structural cross-section of the Songliao Basin (Feng et al., 2010) and (d) sedimentary facies map (Liu et al., 2021).

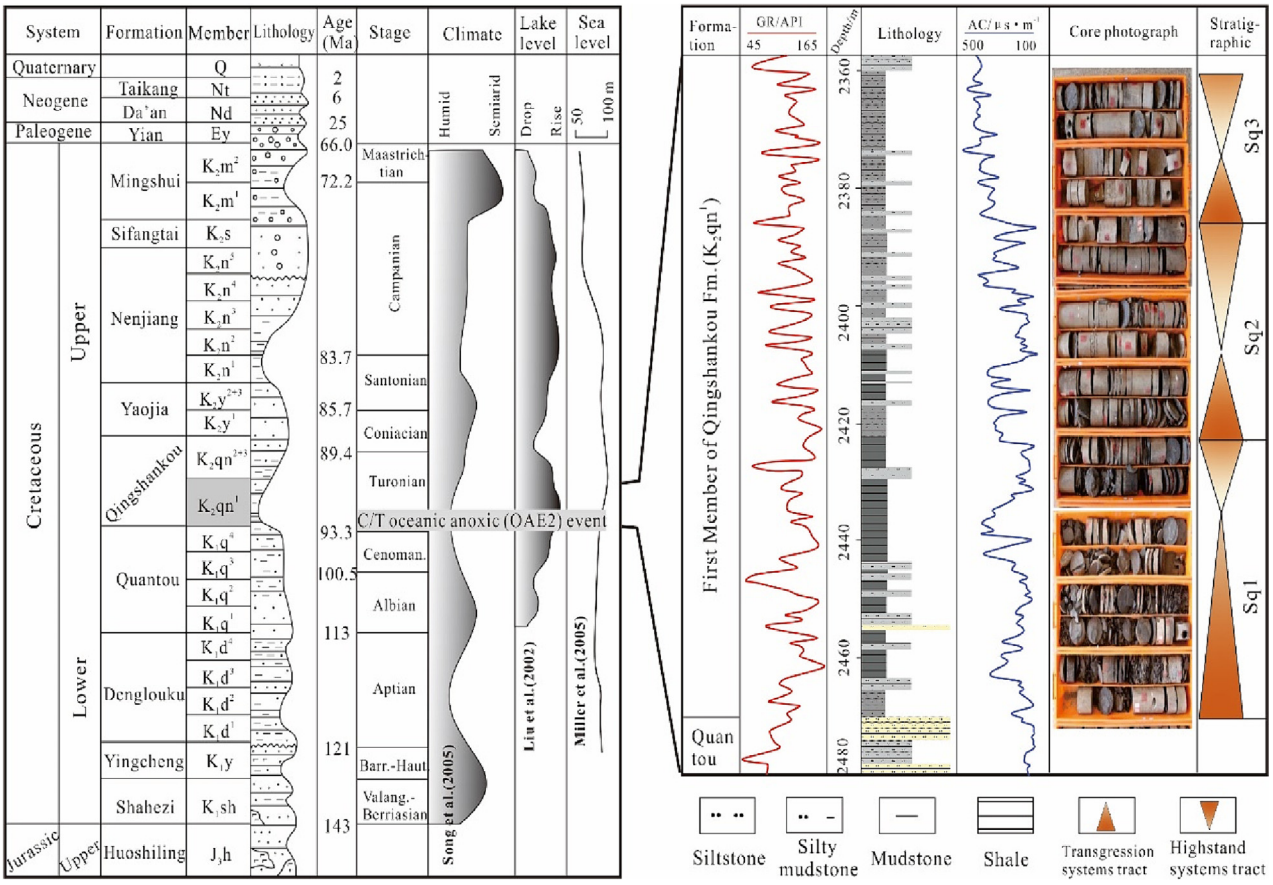


**Fig. 2.** Lithostratigraphy and sequence stratigraphy of the $K_2qn^1$.

tetraborate ($Li_2B_4O_7$) were introduced, fused into glass beads, and subjected to analysis using a PANalytical PW2424 X-ray fluorescence (XRF) spectrometer. The analytical error remained below 5 %. Trace element analysis involved two batches. One batch underwent examination with an Agilent VISTA plasma emission spectrometer (ICP–AES) and an Agilent 7900 inductively coupled plasma mass spectrometer (ICP–MS) following the addition of perchloric acid, nitric acid, and hydrofluoric acid. Another batch was added with $LiBO_2/Li_2B_4O_7$ solvent and then melted at 1025 °C. After cooling down, it was analyzed by an Agilent 7900 inductively coupled plasma mass spectrometer (ICP–MS). The concentrations of trace elements were derived by averaging the results from the two analyses, which gave an error of <10 %.

### 3.5. Organic petrography

Microscopic observations were conducted using a Leica DM6000M microscope. For detailed examination, polished sections of the samples were immersed in oil (with a refractive index of 1.518) for the examination under an optical microscope. During the analysis, both white light and fluorescence illumination methods were employed for the identification of microscopic components (Flores et al., 2010). Maceral composition analysis was carried out using reflected white and fluorescent light under a 50× objective. A total of 500 points per polished block were counted using the singlescan method (Zhang et al., 2021).

### 3.6. Biomarker analysis

Saturated hydrocarbon analysis was performed using a Clarus 500 gas chromatography-mass spectrometer, which was equipped with an HP-5MS fused silica capillary column (60 m × 0.25 mm × 0.25 μm). The specific chromatographic temperature program implemented was 80 °C–150 °C–310 °C. Helium served as the carrier gas (Misch et al., 2015). Before analysis (Fowler et al., 1995), the extracted soluble organic matter underwent processing with chloroform/methanol (87:13, v/v). It was then separated into saturated hydrocarbons, aromatic hydrocarbons, and polar compounds (including asphaltenes). The saturated fraction was subsequently dissolved in hexane for gas chromatography-mass spectrometer analysis.

## 4. Results

### 4.1. Lithology and sedimentary characteristics

Detailed descriptions, photographs, and sediment particle size analysis from 107 m of core samples that penetrated the $K_2qn^1$ are shown in Fig. 2. The lithology of the Sq1 phase is predominantly characterized by black shales, which frequently intercalated by silty intervals. The Sq2 and Sq3 phases are primarily composed of gray–black shales, interspersed with thin layers of gray silty mudstones. Multiple sedimentary intervals composed of both normal grading and inverse grading in ascending order can be observed over the depth of 2430–2440 m. At a macroscopic level, with an average thickness of around 0.9 cm, the demarcation between the lower reverse grading and upper normal grading is clearly discernible. This boundary is characterized by the presence of the highest concentration of larger clasts and a slightly lighter coloration in the central region. Nevertheless, internal wave erosional surfaces and microerosional surfaces can still be observed (Fig. 3a), which are possibly related to the intensity of event-driven deposition or erosion during rapid rise of lake level (Yang et al., 2017).

The alterations in color and grain size are more distinctly observable in thin sections than in core samples. Under a microscope, the boundaries between normal grading and inverse grading become distinct, and the grain

size and clay component become easily discernible. The coarsest quartz grains are concentrated at the level separating normal grading from inverse grading (Fig. 3b). As the interval transits from inverse grading to normal grading, the content of coarse quartz grain increases, with individual grain diameters reaching their maximum. In the zones between each erosional surface, the highest concentrations of coarsest quartz grains and organic matter are noted to be higher (Fig. 3b, c). These erosional surfaces can be classified into two types: wavy bedding and low-amplitude wavy bedding. The interlayer erosional surfaces are present (Fig. 3b), but erosional contacts within the sequence are unclear or missing, and the interfaces between layers are nearly parallel (Fig. 3c).

### 4.2. Mineralogical features

The mineral assemblage primarily consists of quartz (13.8 % to 76.6 %; avg. 38.0 %), clay minerals (10.4 % to 60.4 %; avg. 43.1 %), and pyrite (0.6 % to 4.7 %; avg. 2.0 %), with minor amounts of carbonate minerals (such as calcite, dolomite, siderite) (Fig. 4a). The quartz content in the Sq3 phase (avg. 49.0 %) is much higher than those in the Sq2 phase (avg. 39.0 %) and the Sq1 phase (avg. 34.7 %). The clay content (avg. 45.5 %) and pyrite content (avg. 2.2 %) in the Sq1 phase are only slightly higher than the other phases (Fig. 4a). The lithofacies types are siliceous shale and argillaceous shale, with argillaceous shale exhibiting higher TOC content (Fig. 4b).

### 4.3. Major and trace element characteristics

Table 1 presents the major and trace element data. The four major elements are $SiO_2$ (avg. 55.8 %), $Al_2O_3$ (avg. 16.5 %), $Fe_2O_3$ (avg. 5.4 %), and CaO (avg. 2.6 %). When compared with the average major element concentrations of the upper continental crust (UCC), the $K_2qn^1$ shale has lower contents of MgO (avg. 2.3 %), CaO (avg. 2.6 %),

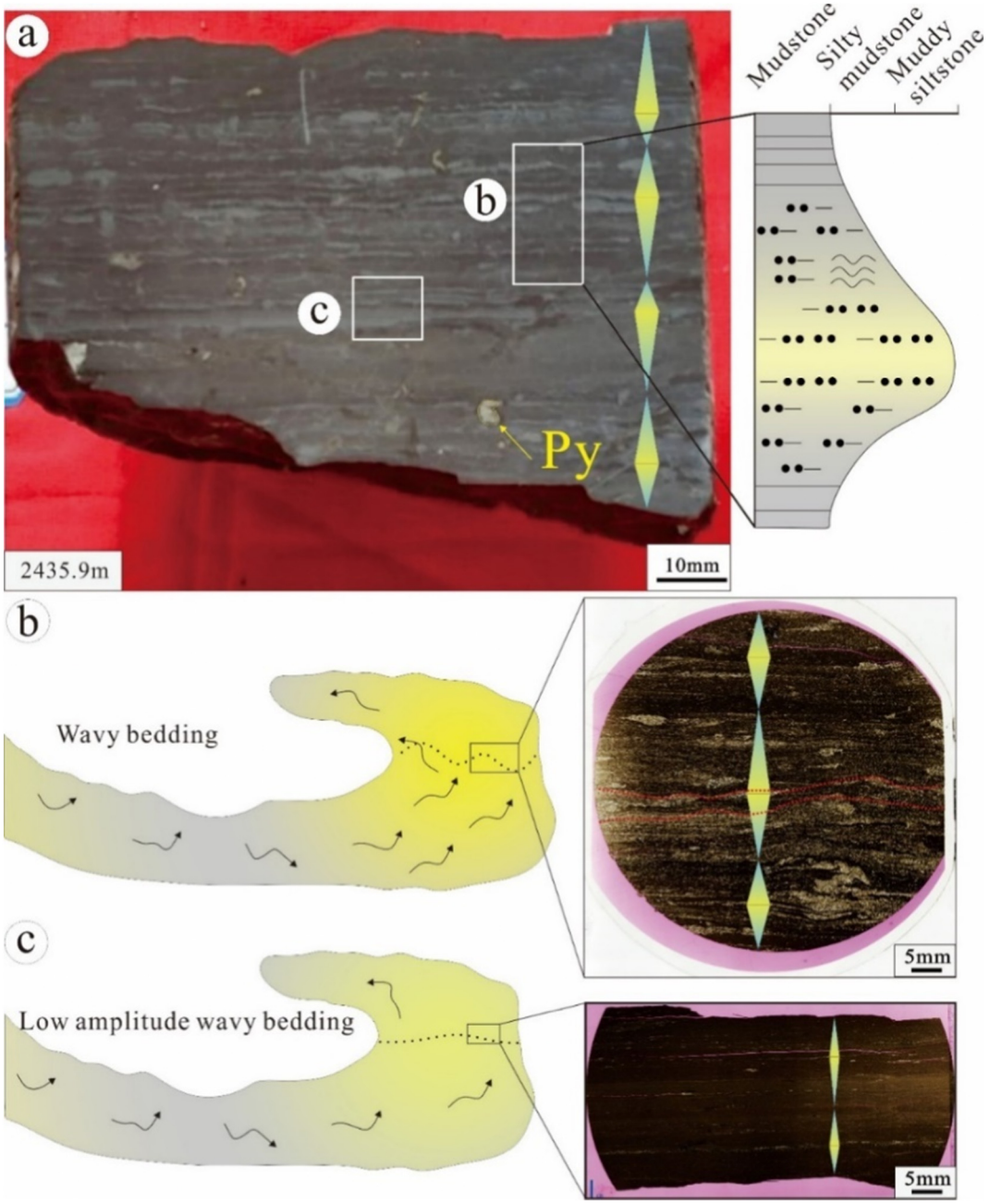


**Fig. 3.** Sedimentary macroscopic characteristics and micro features of the $K_2qn^1$.

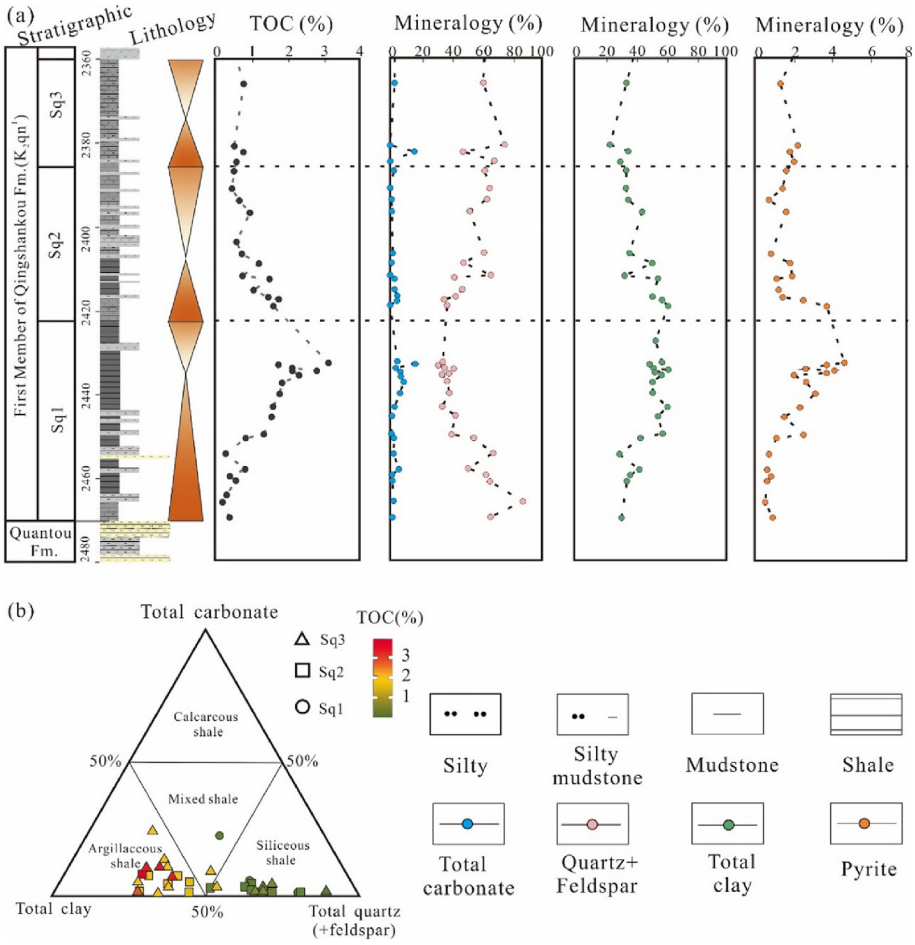


**Fig. 4.** Characteristics of shale lithofacies of the $K_2qn^1$. (a) Whole-rock mineral distribution characteristics of the $K_2qn^1$; (b) triangular plot of whole-rock mineral composition of the $K_2qn^1$.

and $P_2O_5$ (avg. 0.13 %), while the contents of $SiO_2$ and $Al_2O_3$ are close to the UCC values.

The major large ion lithophile elements (Rb, Sr, Th, U, Ba) show similar concentrations to the UCC, except for a slight depletion in Sr. However, the transition metal elements (Ni, V, Cr, Co, and Cu) show relatively weak enrichment. The element with the highest concentration in the samples is Ba, ranging from 349 to 732 μg/g (avg. 448.55 μg/g). While most trace elements show relatively constant concentrations, Cu, Sr, and Ba exhibit significant variations. The Ba content in the Sq1 phase (avg. 437.6 μg/g) is higher than those in the Sq2 phase (avg. 439 μg/g) and the Sq3 phase (avg. 361.5 μg/g); the Sr content in the Sq1 phase (avg. 349.4 μg/g) is also slightly higher.

**Table 1**
Major and trace element compositions of the $K_2qn^1$.

| Phase | Depth/m | Major elements (%) | | | | | | | | Trace elements (μg/g) | | | | | | | | | | | |
|---|---|---|---|---|---|---|---|---|---|---|---|---|---|---|---|---|---|---|---|---|---|
| | | $SiO_2$ | $Al_2O_3$ | $TiO_2$ | $P_2O_5$ | $Fe_2O_3$ | CaO | MgO | LOI | Ba | Zr | Sr | Rb | Zn | Cu | Ni | Cr | V | Co | Th | U |
| Sq3 | 2361.03 | 49.25 | 14.71 | 0.34 | 0.06 | 5.31 | 7.52 | 3.54 | 9.87 | 351.00 | 189.00 | 296.00 | 142.90 | 152.10 | 34.10 | 32.70 | 30.90 | 124.70 | 6.40 | 10.10 | 7.90 |
| | 2368.40 | 56.19 | 17.11 | 0.38 | 0.07 | 5.76 | 2.33 | 2.14 | 12.86 | 372.00 | 197.00 | 317.00 | 169.80 | 143.00 | 32.90 | 30.80 | 29.40 | 120.70 | 6.10 | 10.10 | 7.30 |
| Sq2 | 2399.20 | 57.27 | 17.94 | 0.66 | 0.13 | 5.60 | 0.89 | 2.06 | 9.06 | 415.00 | 218.00 | 260.00 | 178.60 | 140.70 | 30.70 | 31.40 | 30.50 | 128.50 | 5.80 | 7.00 | 5.40 |
| | 2401.90 | 58.50 | 17.71 | 0.78 | 0.28 | 3.93 | 1.11 | 1.85 | 7.47 | 432.00 | 259.00 | 301.00 | 176.50 | 137.40 | 28.70 | 25.00 | 30.20 | 130.10 | 4.50 | 10.70 | 9.10 |
| | 2411.10 | 53.34 | 15.28 | 0.37 | 0.08 | 4.76 | 6.67 | 1.96 | 8.93 | 418.00 | 205.00 | 334.00 | 154.40 | 116.60 | 27.10 | 29.80 | 27.60 | 107.50 | 5.10 | 12.60 | 10.60 |
| | 2411.86 | 55.49 | 16.48 | 0.64 | 0.18 | 5.17 | 2.99 | 2.15 | 11.04 | 438.00 | 201.00 | 406.00 | 173.40 | 125.60 | 30.80 | 28.50 | 29.10 | 108.00 | 4.90 | 11.10 | 10.20 |
| | 2412.80 | 57.80 | 17.60 | 0.41 | 0.06 | 4.42 | 1.36 | 1.94 | 9.30 | 472.00 | 231.00 | 306.00 | 178.80 | 125.40 | 30.80 | 28.80 | 28.60 | 121.00 | 5.40 | 11.30 | 10.30 |
| | 2416.70 | 55.95 | 15.09 | 0.35 | 0.07 | 6.38 | 3.28 | 2.23 | 9.05 | 418.00 | 190.00 | 438.00 | 142.30 | 166.20 | 64.60 | 32.20 | 20.40 | 86.60 | 6.40 | 7.90 | 6.20 |
| | 2419.50 | 55.56 | 16.03 | 0.61 | 0.14 | 5.39 | 3.53 | 2.19 | 10.06 | 453.00 | 199.00 | 480.00 | 157.70 | 108.20 | 29.90 | 26.60 | 26.90 | 109.80 | 4.70 | 9.30 | 7.80 |
| | 2421.50 | 56.46 | 17.71 | 0.45 | 0.07 | 5.76 | 0.85 | 2.35 | 9.71 | 466.00 | 229.00 | 270.00 | 183.00 | 126.70 | 38.80 | 33.40 | 35.90 | 128.50 | 5.60 | 11.40 | 14.90 |
| Sq1 | 2431.50 | 55.17 | 14.57 | 0.36 | 0.08 | 6.33 | 2.65 | 2.26 | 8.67 | 545.00 | 191.00 | 362.00 | 123.90 | 100.30 | 44.00 | 28.60 | 21.00 | 114.00 | 4.70 | 5.10 | 7.10 |
| | 2436.10 | 55.77 | 16.49 | 0.62 | 0.51 | 6.44 | 1.49 | 2.37 | 11.54 | 349.00 | 203.00 | 316.00 | 161.20 | 127.10 | 39.20 | 36.10 | 35.10 | 122.70 | 4.70 | 8.00 | 11.10 |
| | 2440.10 | 54.75 | 16.30 | 0.40 | 0.07 | 6.49 | 2.76 | 2.73 | 8.61 | 381.00 | 202.00 | 353.00 | 176.80 | 112.00 | 28.30 | 33.20 | 26.90 | 116.60 | 3.40 | 11.70 | 15.10 |
| | 2441.00 | 51.79 | 13.69 | 0.35 | 0.08 | 7.02 | 6.69 | 2.61 | 9.59 | 431.00 | 178.00 | 357.00 | 120.30 | 141.10 | 26.60 | 30.00 | 29.10 | 122.60 | 6.30 | 10.10 | 12.80 |
| | 2442.40 | 56.87 | 17.98 | 0.71 | 0.20 | 4.68 | 1.22 | 2.16 | 11.79 | 466.00 | 219.00 | 278.00 | 176.70 | 118.90 | 34.20 | 30.30 | 27.70 | 126.40 | 3.40 | 12.40 | 15.30 |
| | 2447.10 | 55.79 | 17.94 | 0.70 | 0.15 | 4.42 | 1.12 | 2.09 | 8.32 | 732.00 | 272.00 | 253.00 | 161.30 | 121.20 | 27.80 | 30.40 | 25.50 | 115.90 | 3.70 | 9.00 | 11.40 |
| | 2451.10 | 57.08 | 17.90 | 0.45 | 0.06 | 4.81 | 1.70 | 2.28 | 10.76 | 424.00 | 229.00 | 272.00 | 196.90 | 129.00 | 33.80 | 28.90 | 21.60 | 130.20 | 2.90 | 11.10 | 13.80 |
| | 2457.59 | 58.08 | 13.97 | 0.64 | 0.15 | 5.29 | 1.57 | 2.06 | 8.65 | 371.00 | 259.00 | 233.00 | 124.20 | 91.50 | 17.90 | 26.30 | 25.50 | 129.70 | 3.60 | 8.40 | 9.10 |
| | 2459.59 | 57.12 | 17.56 | 0.38 | 0.06 | 5.20 | 1.48 | 2.07 | 12.23 | 396.00 | 229.00 | 248.00 | 185.70 | 107.90 | 27.50 | 25.10 | 28.30 | 121.00 | 3.70 | 11.40 | 14.10 |
| | 2463.90 | 57.97 | 17.43 | 0.43 | 0.06 | 4.83 | 1.54 | 2.00 | 9.02 | 641.00 | 223.00 | 278.00 | 179.30 | 117.30 | 31.10 | 27.90 | 22.70 | 127.00 | 3.50 | 8.10 | 6.20 |

### 4.4. Bulk geochemical parameters

The TOC contents range from 0.23 % to 3.14 % (avg. 1.24 %), and the HI ranges from 80 mg HC/g to 640 mg HC/g (avg. 265 mg HC/g). The $T_{max}$ values range from 439 °C to 457 °C (avg. 446 °C). It can be inferred from the HI and $T_{max}$ values that the kerogen is primarily of Types II and II/III, with localized development of Type I in the Sq1 phase (Fig. 5a). The TOC and $S_2$ values also confirm that the kerogen is primarily Types II and II/III (Fig. 5b, c).

### 4.5. Organic compound distributions

Table 2 shows that the distribution pattern of regular steranes follows the order of C29 > C27 > C28, with the concentrations of C29 steranes ranging from 25 % to 60 % (avg. 47 %), C28 steranes from 11 % to 66 % (avg. 38 %), and C27 steranes from 2 % to 61 % (avg. 15 %). The gammacerane index (GI = gammacerane/C30 hopane) also displays variability, with the highest GI values (0.05 to 0.63; avg. 0.22) in the Sq1 phase, followed by a range of 0.07 to 0.28 (avg. 0.16) in the Sq2 phase, and the lowest range of 0.13 to 0.14 (avg. 0.135) in the Sq3 phase.

## 5. Discussion

### 5.1. Source of organic matter

Regular steranes primarily originate from sterols, with C27 steranes mainly from phytoplankton, C28 steranes from algae, and C29 steranes from terrestrial plants (Cheng et al., 2019). The relative proportions of these regular steranes have been utilized to determine the source of organic matter. In the C27-C28-C29 regular sterane source discrimination diagram, our samples mostly fall in the terrestrial plant domain with a few in the mixed source domain (Fig. 6a). In the Sq1 phase, kerogen is of humic and sapropelic type, further indicating significant contribution of components from terrestrial higher plants to the TOC (Ardakani et al., 2022). Tricyclic terpane is also a common biomarker for sedimentary environment analysis (Dahl et al., 1993). On the tricyclic terpane ternary diagram (Xiao et al., 2018), our data suggest that the development environments of the source rock were mainly freshwater/brackish terrestrial facies and delta facies (Fig. 6b). The Sq1 phase shows some local marine transgression effects, but it is dominated by C19 + 20 TT, implying that the depositional environment of the source rock was likely deltaic conditions with a high input of terrigenous material (Fig. 6b).

From the perspective of organic petrology, liptinites mainly originate from algae, whereas vitrinite and inertinite primarily represent higher plants (Flores, 2002; Flores et al., 2010; Liu et al., 2017, 2020). Therefore, the relative abundances of maceral composition can be employed to qualitatively assess the source of organic matter (Flores, 2002). The maceral composition of the Sq1 shale is characterized by a dominance of vitrinite (avg. 59 %), followed by liptinite (avg. 23 %) and inertinite (avg. 18 %) (Table 2). This confirms that organic matter sourced from terrestrial higher plants is rich in the Sq1 phase (Dai et al., 2020).

### 5.2. Paleoenvironmental conditions

#### 5.2.1. Paleoredox

The redox state of the environment influences the enrichment of redox-sensitive elements such as Mo, U, V, Cr and Ni in sediments. Consequently, the content or ratios of these elements in sediments can be utilized to assess the redox state (Jones and Manning, 1994). Normally, Ni/Co, V/Cr, and U/Th ratios are considered more reliable than the contents of individual elements. A reducing (anoxic) state can be inferred when U/Th > 1.25, V/Cr > 4.25, or Ni/Co > 7, whereas U/Th < 0.75, V/Cr < 2, or Ni/Co < 5 reflects an oxidizing environment. Ratios falling between correspond to a dysoxic environment (Jones and Manning, 1994). As shown in Fig. 7, the Sq1 samples show data ranges from 3.49 to 6.03 for V/Cr, 4.77 to 9.97 for Ni/Co, and 0.77 to 1.39 for U/Th, implying a general dysoxic–anoxic condition. In the Sq2 and Sq3 samples, the data range from 3.58 to 4.31 for V/Cr, 5.03 to 5.96 for Ni/Co, and 0.72 to 1.31 for U/Th, indicative of a dysoxic environment.

Furthermore, the distribution of framboidal pyrite has also been widely used as an indication of redox conditions (Wilkin et al., 1996; Zhang et al., 2022). The rate of the pyrite precipitation process is closely linked to the extent of bottom water anoxia. Consequently, the size and shape features of framboidal pyrite act as a conspicuous indicator of redox conditions. Pyrite framboids that originate in strongly anoxic environments show smaller but more evenly dispersed characteristics compared with those formed in oxic/dysoxic bottom waters (Huang

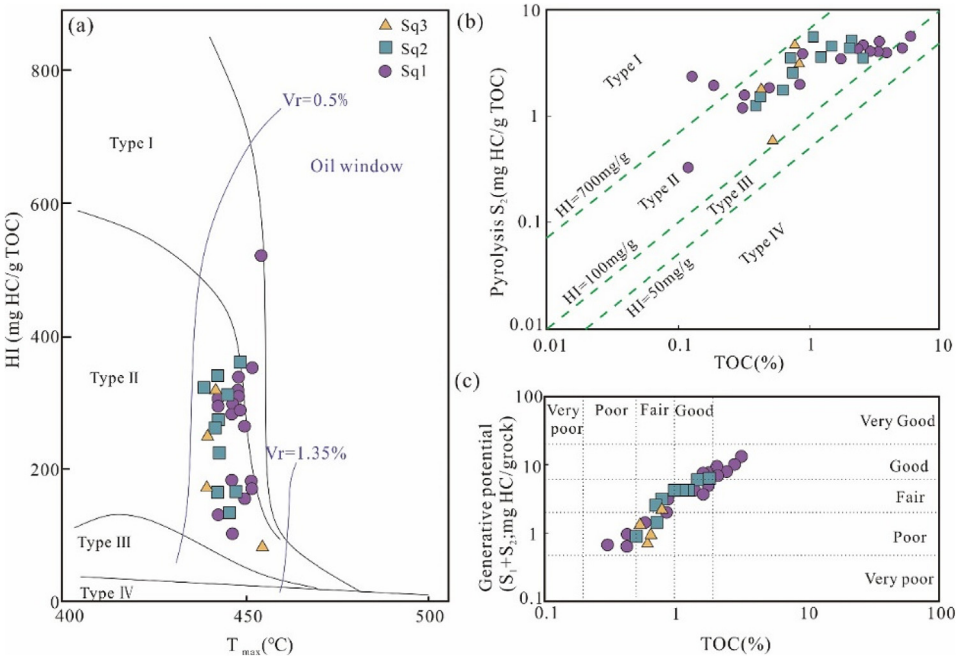


**Fig. 5.** (a) Plot of $T_{max}$ versus hydrogen index; (b) plot of the pyrolysis $S_2$ and TOC content; (c) plot of $S_1 + S_2$ and TOC content (Peters, 1986; Peters and Cassa, 1994).

**Table 2**
Maceral content and biomarker parameters of the $K_2qn^1$.

| Phase | Depth/m | Maceral composition (%) | | | GI | Regular steranes distribution (%) | | | Tricyclic terpane (TT, %) | | |
|---|---|---|---|---|---|---|---|---|---|---|---|
| | | Liptinite | Vitrinite | Inertinite | | 20R C27 | 20R C28 | 20R C29 | C19 + 20TT | C21TT | C23TT |
| Sq3 | 2361.03 | 22 | 51 | 27 | 0.13 | 37 | 20 | 43 | 31 | 50 | 19 |
| | 2368.40 | 21 | 51 | 28 | 0.14 | 8 | 31 | 60 | 26 | 41 | 33 |
| Sq2 | 2399.20 | 18 | 74 | 8 | / | 23 | 34 | 43 | 53 | 21 | 27 |
| | 2401.90 | 12 | 54 | 34 | 0.28 | 13 | 37 | 50 | 21 | 34 | 45 |
| | 2411.10 | 25 | 34 | 41 | 0.07 | 10 | 47 | 42 | 34 | 35 | 31 |
| | 2411.86 | 22 | 50 | 28 | 0.07 | 46 | 18 | 37 | 48 | 17 | 35 |
| | 2412.80 | 23 | 57 | 20 | 0.18 | 8 | 33 | 59 | 47 | 19 | 34 |
| | 2416.70 | 21 | 63 | 16 | / | 16 | 41 | 43 | 53 | 23 | 24 |
| | 2419.50 | 26 | 46 | 28 | 0.19 | 3 | 47 | 50 | 34 | 32 | 34 |
| Sq1 | 2431.50 | 20 | 70 | 10 | 0.14 | 3 | 46 | 51 | 46 | 23 | 31 |
| | 2436.10 | 26 | 62 | 12 | 0.63 | 3 | 47 | 50 | 18 | 40 | 42 |
| | 2440.10 | 15 | 48 | 37 | 0.44 | 11 | 42 | 47 | 44 | 26 | 29 |
| | 2441.00 | 17 | 67 | 16 | 0.21 | 14 | 40 | 46 | 52 | 22 | 26 |
| | 2442.40 | 24 | 50 | 26 | 0.21 | 3 | 45 | 52 | 19 | 38 | 44 |
| | 2447.10 | 20 | 70 | 10 | 0.20 | 17 | 33 | 50 | 52 | 19 | 29 |
| | 2451.10 | 23 | 67 | 10 | 0.31 | 8 | 36 | 56 | 41 | 23 | 36 |
| | 2453.00 | 18 | 60 | 22 | 0.13 | 9 | 66 | 25 | 54 | 14 | 32 |
| | 2457.59 | 45 | 45 | 11 | 0.13 | 7 | 51 | 41 | 49 | 17 | 33 |
| | 2459.59 | 21 | 59 | 20 | 0.05 | 13 | 36 | 51 | 52 | 20 | 28 |
| | 2463.90 | 19 | 63 | 18 | 0.18 | 7 | 36 | 59 | 46 | 20 | 34 |
| | 2468.56 | 34 | 54 | 13 | 0.17 | 61 | 12 | 27 | 60 | 12 | 28 |
| | 2469.70 | 23 | 50 | 27 | 0.06 | 3 | 50 | 47 | 25 | 39 | 36 |

et al., 2019; Zhang et al., 2022). The size of framboidal pyrites in the Sq2 and Sq3 phases is generally larger, ranging from 2.1 to 9.8 μm (avg. 4 μm), with very few framboidal aggregates <2 μm in diameter. The size standard deviation values range from 2 to 4. In contrast, in the upper part of the Sq1 phase, framboidal pyrites are abundant but small, with diameters ranging from 0.5 to 4.5 μm (Fig. 8). When plotted on the environmental discrimination diagram, the samples from the Sq2 and Sq3 phases fall within the dysoxic area, while the sample from the Sq1 phase lands in the anoxic area.

In summary, based on whole-rock trace element data and size distribution of framboidal pyrite, we can infer that the redox conditions at the bottom of the Sq1 phase was oxidic with a transition to anoxic conditions toward the top, and gradually changed from anoxic to dysoxic conditions in the Sq2 and Sq3 phases (Fig. 9).

*5.2.2. Water salinity*

Water stratification commonly occurs in saline environments, resulting in anoxic layers that are conducive to the preservation of organic matter. This stratification is strongly dependent on salinity levels, which are positively correlated to the GI values (Moldowan et al., 1985). The GI values of the Sq1 phase are highest (between 0.04 and 0.62; avg. 0.22), drop to 0.07 to 0.28 (avg. 0.16) in the Sq2 phase, and display lowest values in the Sq3 phase (between 0.13 and 0.14; avg. 0.135). The overall GI ranges of these phases indicate that the sampled sediments were primarily deposited in a slightly saline water environment, with high TOC shales mainly developed in saline environments (Fig. 10).

The Sr/Ba ratio of sediment is another effective salinity indicator (Remírez and Algeo, 2020; Wei and Algeo, 2020). It increases with the salinity of water body, as the formation of $SrSO_4$ precipitates requires higher salinity conditions than $BaSO_4$ precipitates (Zeng et al., 2015). Salinity of sedimentary environments can be distinguished by Sr/Ba values of >1 for saline, 0.5–1 for brackish, and <0.5 for freshwater, respectively (Li et al., 2020). It is important to note that the premise to use Sr/Ba values as a paleosalinity indicator is that Sr in sediments is primarily associated with clays rather than carbonates, as carbonates can store significantly more Sr than clays (Remírez and Algeo, 2020). The studied samples have a very low carbonate content (Fig. 4a), and thus the amount of strontium sequestered in carbonates is minimal.

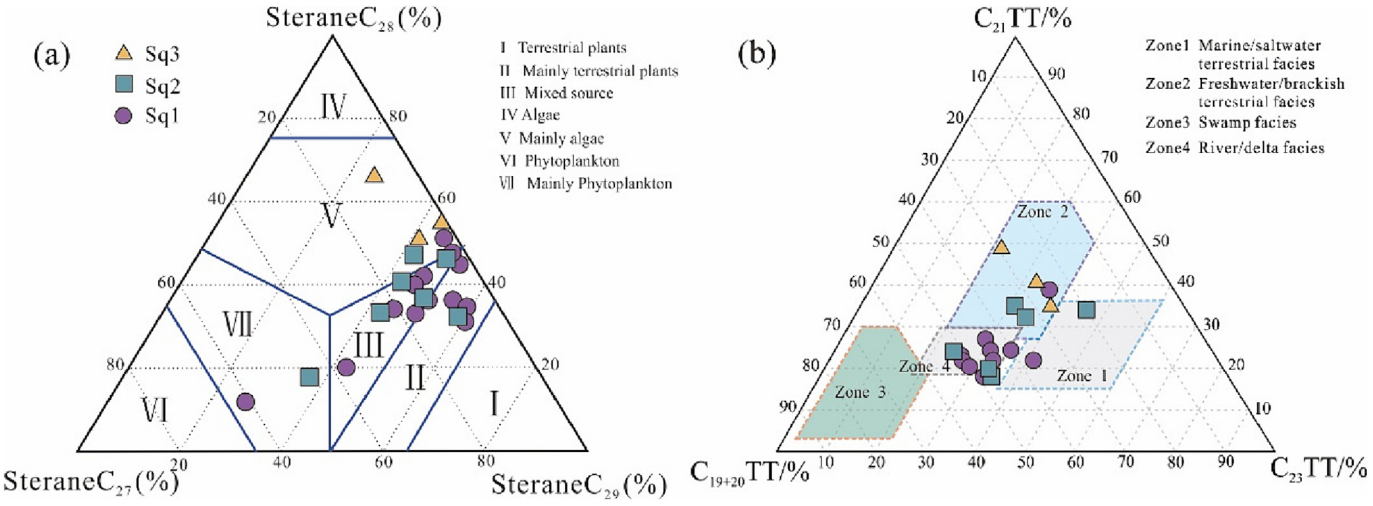


**Fig. 6.** (a) A ternary diagram of relative abundance of $C_{27}$-$C_{28}$-$C_{29}$ αααα R steranes (Cheng et al., 2019); (b) a ternary diagram of relative abundance of $C_{19+20}$TT, $C_{21}$TT, and $C_{23}$TT of the $K_2qn^1$ (Xiao et al., 2018).

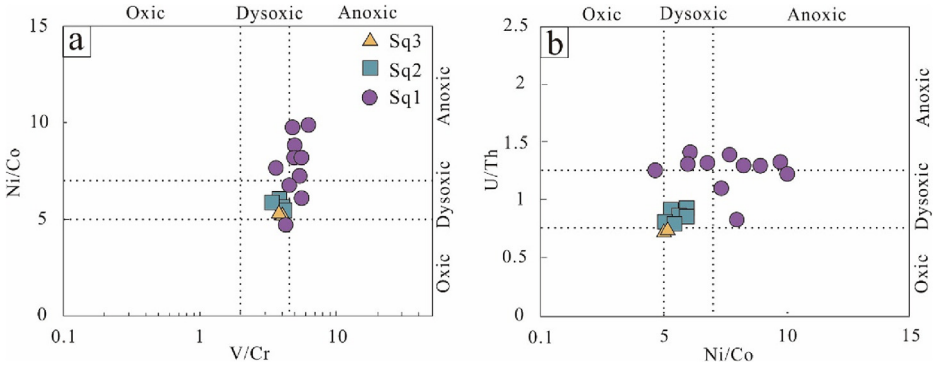


**Fig. 7.** Redox discrimination diagram for the $K_2qn^1$. (a) V/Cr versus Ni/Co; (b) Ni/Co versus U/Th (Jones and Manning, 1994; Wignall and Twitchett, 1996; Rimmer, 2004; Tribovillard et al., 2006).

Therefore, the Sr/Ba paleosalinity indicator can be applied to our samples. The Sr/Ba ratios of the studied samples (0.35 to 1.35; avg. 0.77) suggest that the $K_2qn^1$ was deposited in a brackish–freshwater environment, and high TOC shales were mainly formed in saline conditions (Fig. 10).

*5.2.3. Paleoclimate*

Paleoclimate can significantly impact the paleoproductivity and preservation of organic matter. To understand paleoclimatic effect, trace element data can provide important insights (Chen et al., 1999; Yandoka et al., 2015). For example, elements such as Fe, V, Ni, Cu, and Co are highly soluble in water during warm and humid climatic conditions, and thus can be used to trace climatic variations (Martinez-Ruiz et al., 2015). In addition, Sr/Cu and Rb/Sr ratios are also commonly used to infer past climatic conditions with $1 < Sr/Cu < 10$ and $Rb/Sr < 0.5$ typically indicating a humid climate, whereas $Sr/Cu > 10$ and $Rb/Sr > 0.5$ indicating a dry and hot climate (Yandoka et al., 2015; Song et al., 2016).

The Sr/Cu ratios of the Sq1 samples are less than or equal to 10 in about half of the samples (Fig. 10), which strongly suggests that the paleoclimatic conditions in that period were generally warm and humid. This interpretation is consistent with previous studies which reported high Sr/Cu ratios in the southeastern uplift of the Songliao Basin (Jia et al., 2013). Furthermore, the low Rb/Sr ratios of the studied samples (0.16–0.75; avg. 0.52), indicative of differential mobilization of elements from the parent rocks during chemical weathering, corroborate these interpretations and are consistent with previous studies (Wu et al., 2023).

*5.2.4. Terrigenous input*

Terrigenous clastics, as one of the most important sources of sediments, are considered to be one of the key factors affecting the composition of black shales as well as the accumulation and preservation of organic matter (Ibach, 1982; Wu et al., 2023). Specifically, terrigenous clastics can act as diluent to decrease organic content, but the clay component can act as an adsorbent to enrich organic content. Thus, the influence of terrigenous input on the depositional environment must be considered when studying the aggregation and preservation of organic matter (Wu et al., 2023). Elements such as Al, Ti, and Zr have high chemical stability and are least affected by weathering during sediment transport and deposition (Tribovillard et al., 2006), making them reliable indicators of terrigenous input.

The high content of Al (avg. 9.06 %) at the bottom of the Sq1 phase could be potentially attributed to a relatively low lake level (Ghienne, 2003). Subsequently, the terrigenous input significantly decreased in the upper part of the Sq1 phase (avg. 8.08 %), suggesting a notable rise in the lake level by that time. In the Sq2 and Sq3 phases, the Al content gradually increases (Fig. 10), which indicates a sustained long-term

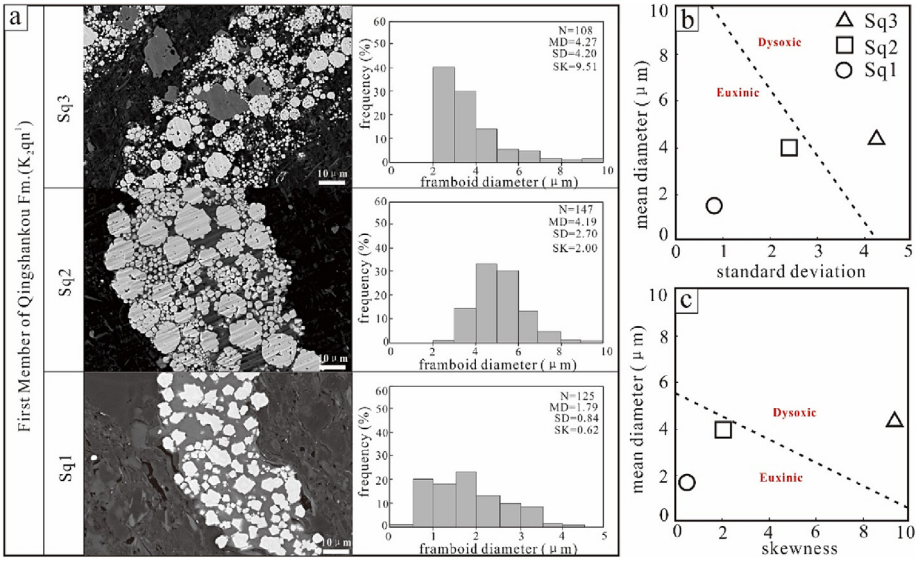


**Fig. 8.** (a) Size distribution of the framboidal pyrite; (b) the standard deviation; and (c) skewness of the distribution, respectively, pointing toward euxinic/anoxic or dysoxic conditions.

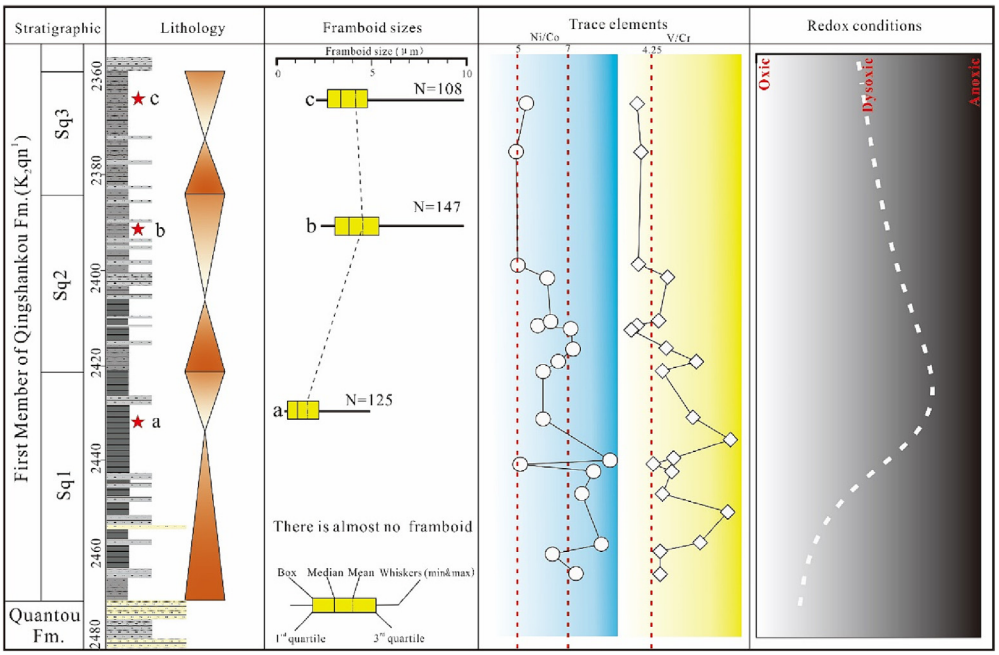


**Fig. 9.** Evolution of redox conditions inferred from framboid pyrite size distributions and trace elements of the $K_2qn^1$.

increase in clastic input. The variations in the Ti content curve are consistent with those in the Al content curve (Fig. 10), demonstrating an initial decrease followed by an increase in detrital input.

### 5.3. Sedimentary formation model of organic matter

The Upper Cretaceous Qingshankou Formation in the Songliao Basin was deposited in a large depression lake basin associated with a large-scale water inflow. This lake basin featured a wide expansion and a deep to semi-deep water column, leading to the deposition of thick layers of dark mudstone and shale enriched in organic matter (Liu et al., 2021; Zhang et al., 2022; Wu et al., 2023). The $K_2qn^1$ exhibits a vertical deltaic progradation trend, transitioning from deep-lake to semi-deep-lake conditions (Fig. 11).

The Sq1 deposition period corresponds to the lake flooding period, when the water body expanded associated with decreased input of terrestrial materials into the deep lake (Fig. 11a). However, fine-grained sediment can deposit not only under quiet-water, deep-lacustrine

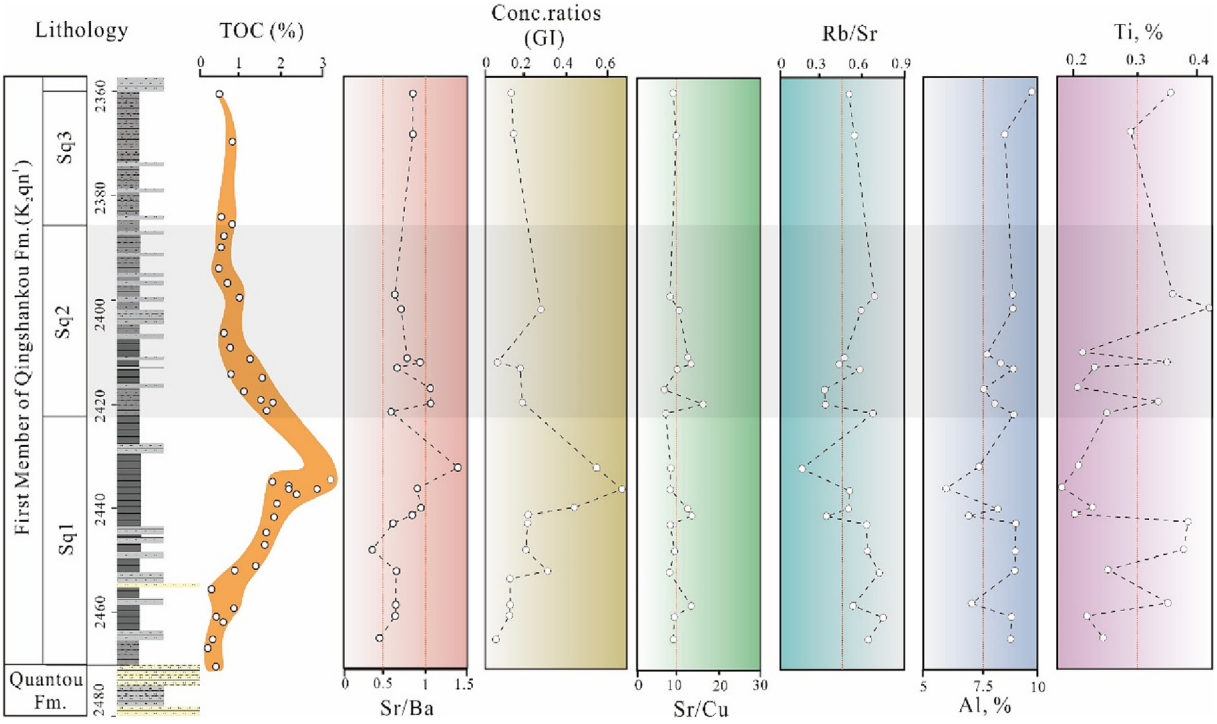


**Fig. 10.** The water salinity, paleoclimate and terrigenous input of the $K_2qn^1$.

depositional environments but also under stronger hydrodynamic conditions (Mulder et al., 2003). The sedimentation event responsible for these features likely signifies flood-generated hyperpycnal flows in a deep lake depositional environment (Fig. 3) (Mulder and Alexander, 2001; Yang et al., 2017; Zou et al., 2023). Intermittent floods under lake invasion conditions could still bring terrestrial materials, and the input of multi-period hyperpycnal flow activities continued to carry a large amount of nutrients and promoted the prosperity of surface plankton. In addition, the higher Sr/Ba value and GI value reflect the higher salinity of the lake water, while the higher Sr/Cu value reflects the warm and humid paleoclimate conditions. The lake water eventually became stratified and conducive to euryhaline organisms and the preservation of organic matter. Furthermore, the deepening of water body resulted in increased water retention, which increased the primary productivity of the water body in this period to a medium level. The shale deposited in this semi-deep to deep lake area was poor in carbonate minerals but rich in clay minerals (Fig. 4). As a result, organic matter was well developed and preserved in deeper water bodies, resulting in high TOC content to the Sq1 phase, which becomes the main source rock in the basin, and currently the main development section of shale oil.

In the Sq2 and Sq3 deposition periods, the lake began to shrink, associated with decreasing water salinity and increasing terrigenous input, which developed interbedded mudstone and siltstone (Fig. 11b).

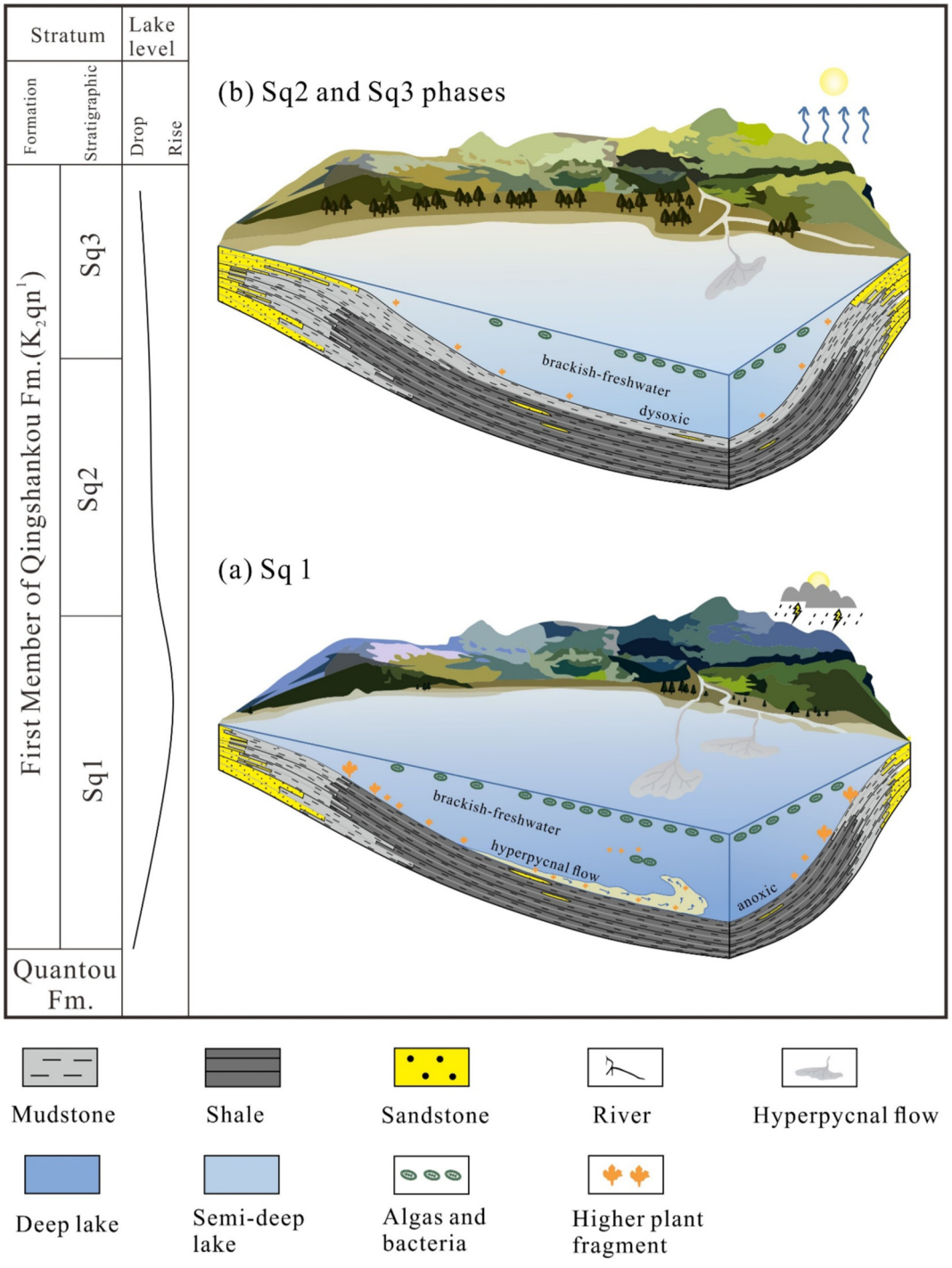


**Fig. 11.** The organic matter accumulation mechanism and formation model of organic matter of the $K_2qn^1$.

Moderate Sr/Ba values and Sr/Cu values indicate moderate salinity and semi-arid paleoclimate conditions with a dysoxic bottom water environment during this period. The lake water stratification was not significant, producing an environment that was less conducive to the survival of aquatic life and the preservation of organic matter (Zhang et al., 2022). The hyperpycnal flow activity during this period was limited and the nutrient elements in the lake basin were insufficiently supplied, restricting the prosperity of organisms to a certain extent. In addition, the high detrital input practically diluted the content of organic matter. Altogether, the relatively low primary productivity and the dilution of inorganic particles resulted in smaller TOC contents in the Sq2 and Sq3 phases than in the Sq1 phase.

### 5.4. Geological preservation of organic matter

The formation of organic-rich shale requires a relatively abundant supply of organic matter. To ensure accumulation, it is crucial that organic matter degradation should not occur too rapidly, neither should be the sedimentation rate of terrigenous clastics too high. Under this context, organic accumulation is favored in muddy sediments under conditions of relatively excessive organic matter supply, relatively slow sedimentation rates, and bottom water oxidation. However, the organic matter settled in sediments can continue to undergo oxidative decomposition or be further degraded by microorganisms through processes such as fermentation, anaerobic respiration, and alkane production (Kennedy et al., 2002; Lalonde et al., 2012; Hemingway et al., 2019). The mechanism to favor the long-term preservation of organic matter in black shales over the degradation processes is not well understood yet.

Our data show that the vertical variations of TOC and total clay mineral contents are highly correlated in the $K_2qn^1$ (Fig. 12). This phenomenon suggests that clay minerals play an important role in the enrichment and long-term preservation of organic matter (Liu et al., 2019b; Murray and Jagoutz, 2024). Furthermore, experimental studies have shown that different types of clays have variable capacities for organic carbon adsorption. For example, each gram of illite–kaolinite clay can adsorb 29.2 mg of organic carbon, each gram of montmorillonite clay can adsorb 77.5 mg of organic carbon, and each gram of hydroaluminosilicate clay can adsorb 123.5 mg of organic carbon (Churchman et al., 2020). Organic matter bound within the interlayers of clay minerals is relatively resistant to oxidation or microbial alteration and thus can be better preserved (Saggar et al., 1996; Brockamp, 2011). When montmorillonite flocculates and settles, some montmorillonite escapes in the form of shed particles, which may subsequently reassemble and sink (Blattmann et al., 2019). Hence, these results imply that, apart from a saline anoxic water environment, the persistence of continentally derived organic matter in lacustrine shale is controlled by clay minerals.

Given that clay minerals are widespread in lacustrine environments and their important role in organic preservation as shown above (Kennedy et al., 2002; Blattmann et al., 2019), we propose a new "source-preservation" enrichment model for shale organic matter (Fig. 13). In this model, the rapid rise of lake level and hyperpycnal flows are crucial for the transport of terrigenous organic matter to the shale depositional environment, where it interacts and mixes thoroughly with clay minerals (Fig. 13b). This interaction leads to the adsorption of recalcitrant dissolved organic carbon by clay minerals. Clay minerals can effectively preserve organic matter in sediments which eventually form organic-rich shale through diagenesis (Fig. 13c).

The new model complements existing models of lacustrine shale deposition and emphasizes the role of clay minerals in preserving organic matter. However, some key parameters, such as the effect of environmental conditions (pH, salinity, temperature, redox conditions) on adsorption efficiency and the effectiveness of different types of clay minerals, remain unknown, which prevents quantitative assessment of organic preservation in shales. It would be necessary to conduct laboratory experiments to determine these parameters in the future.

## 6. Conclusions

This study advanced our understanding of the paleoenvironmental evolution and organic matter enrichment in the $K_2qn^1$, Changling Sag, Songliao Basin. The data yield several key conclusions:

(1) The TOC and S2 values confirm that the kerogen is primarily Types II and II/III. These shales are considered as fair to good hydrocarbon source rocks, with the highest-quality source rock primarily developed in the Sq1 phase. Biomarker and petrographical data indicate that the organic matter of $K_2qn^1$ was mainly from terrigenous plants with some algal input.

(2) Inorganic minerals and petrographical data indicate a warm and humid climate, intense anoxia, and a high degree of salinity stratification in the Changling Sag during most of the organic-rich Sq1 phase. During the Sq2 and Sq3 phases, a relative low lake level and semi-arid climatic conditions prevailed.

(3) These results imply that, apart from a saline anoxic water environment, the persistence of continentally derived organic matter in lacustrine shale is controlled by clay minerals. We proposed a new "source-preservation" enrichment model for lacustrine shale organic matter: The rapid rise of lake level leads to infill of terrigenous organic matter by hyperpycnal flows to the deep

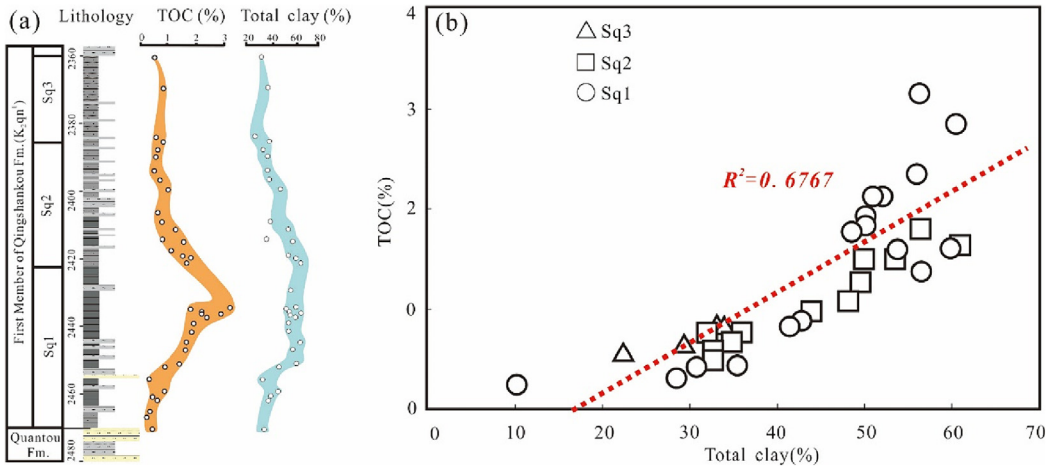


**Fig. 12.** (a) Vertical evolution of TOC and total clay; (b) TOC versus total clay contents of the $K_2qn^1$.

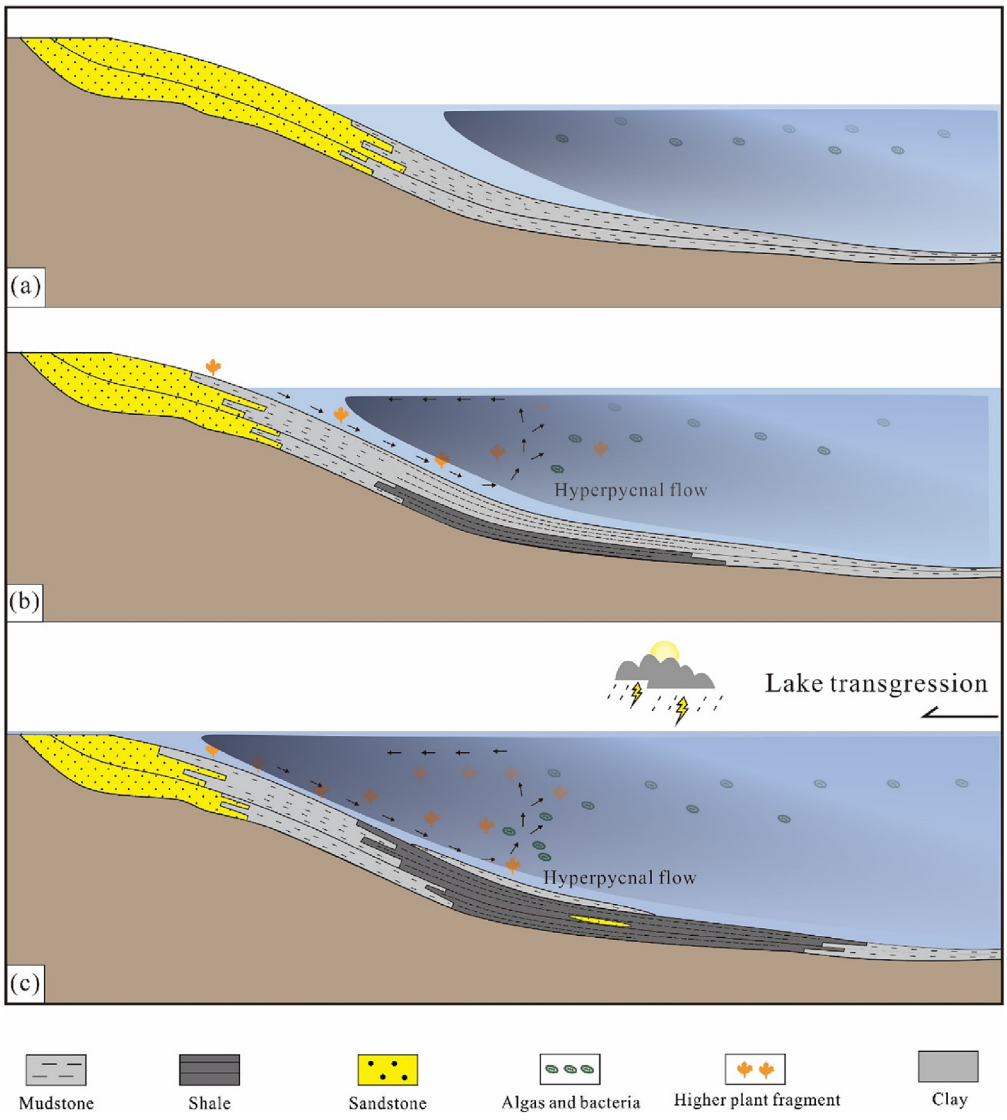


**Fig. 13.** The "source-preservation" enrichment model of organic matter. (a) Before lake transgression; (b) sedimentation of shales driven by hyperpycnal flow of high plant fragment water bodies; (c) sedimentation of organic matter-rich clay sediments following mixture between clays and organic matter during the transgression.

lake, where it is fully mixed with clay minerals. Clay minerals can effectively preserve organic matter in sediments which eventually form organic-rich shales through diagenesis.

## CRediT authorship contribution statement

**Lei Li:** Writing – review & editing, Writing – original draft, Software, Methodology, Data curation, Conceptualization. **Zhidong Bao:** Writing – review & editing, Resources, Project administration, Methodology, Conceptualization. **Long Li:** Writing – review & editing, Writing – original draft, Supervision, Conceptualization. **Zhongcheng Li:** Resources, Conceptualization. **Shuyue Ban:** Software, Data curation. **Zongfeng Li:** Visualization, Validation. **Tengyu Wang:** Visualization, Validation. **Yilin Li:** Software, Investigation. **Naixi Zheng:** Visualization, Validation. **Chenxu Zhao:** Validation, Writing – review & editing. **Li Chen:** Resources, Writing – review & editing. **Jianwen Chen:** Visualization, Resources.

## Data availability

Data will be made available on request.

## Declaration of competing interest

The authors declare that they have no known competing financial interests or personal relationships that could have appeared to influence the work reported in this paper.

## Acknowledgments

This work is jointly funded by the China Scholarship Council (No. 202306440021), and the National Key Research and Development Programs of China (Nos. 2018YFC0604304, 2017YFC0603104). We would like to thank the staff members of Jilin Oilfield for providing the geological data. We also thank Editor-in-chief Dr. Massimo Moretti and two reviewers for their constructive comments.

## References

Abouelresh, M.O., Slatt, R.M., 2012. Lithofacies and sequence stratigraphy of the Barnett Shale in east-central Fort Worth Basin, Texas. AAPG Bulletin 96, 1–22.
Ardakani, O.H., Cesar, J., Pedersen, P.K., Mackie, S.J., Reyes, J., Wood, J.M., 2022. Occurrence and preservation of primary organic matter in a hybrid unconventional reservoir: Montney formation, Western Canada sedimentary basin. International Journal of Coal Geology 261, 104096.

Blattmann, T.M., Liu, Z., Zhang, Y., Zhao, Y., Haghipour, N., Montluçon, D.B., Plötze, M., Eglinton, T.I., 2019. Mineralogical control on the fate of continentally derived organic matter in the ocean. Science 366, 742–745.
Boulila, S., Charbonnier, G., Spangenberg, J.E., Gardin, S., Galbrun, B., Briard, J., Le Callonnec, L., 2020. Unraveling short-and long-term carbon cycle variations during the Oceanic Anoxic Event 2 from the Paris Basin Chalk. Global and Planetary Change 186, 103126.
Brockamp, O., 2011. Delamination of smectite in river-borne suspensions at the fluvial/marine interface—an experimental study. Estuarine, Coastal and Shelf Science 91, 33–41.
Chalmers, G.R., Bustin, R.M., 2008. Lower Cretaceous gas shales in northeastern British Columbia, part I: geological controls on methane sorption capacity. Bulletin of Canadian Petroleum Geology 56, 1–21.
Chen, J., An, Z., Head, J., 1999. Variation of Rb/Sr ratios in the loess-paleosol sequences of central China during the last 130,000 years and their implications for monsoon paleoclimatology. Quaternary Research 51, 215–219.
Cheng, Q., Guanghui, H., Zhang, M., Wenjun, Z., Xi, L., 2019. Distribution and source significance of 2-methylalkanes in coal-measure source rocks, northwest China. Journal of Petroleum Science and Engineering 174, 257–267.
Churchman, G.J., Singh, M., Schapel, A., Sarkar, B., Bolan, N., 2020. Clay minerals as the key to the sequestration of carbon in soils. Clays and Clay Minerals 68, 135–143.
Dahl, J., Moldowan, J.M., Sundararaman, P., 1993. Relationship of biomarker distribution to depositional environment: Phosphoria Formation, Montana, USA. Organic Geochemistry 20, 1001–1017.
Dai, S., Bechtel, A., Eble, C.F., Flores, R.M., French, D., Graham, I.T., Hood, M.M., Hower, J.C., Korasidis, V.A., Moore, T.A., Püttmann, W., Wei, Q., Zhao, L., O'Keefe, J.M.K., 2020. Recognition of peat depositional environments in coal: a review. International Journal of Coal Geology 219, 103383.
Demaison, G., Moore, G., 1980. Anoxic environments and oil source bed genesis. Organic Geochemistry 2, 9–31.
Feng, Z., Fang, W., Wang, X., Huang, C., Huo, Q., Zhang, J., Huang, Q., Zhang, L., 2009. Microfossils and molecular records in oil shales of the Songliao Basin and implications for paleo-depositional environment. Science in China Series D: Earth Sciences 52, 1559–1571.
Feng, Z., Jia, C., Xie, X., Zhang, S., Feng, Z., Cross, T.A., 2010. Tectonostratigraphic units and stratigraphic sequences of the nonmarine Songliao basin, Northeast China. Basin Research 22, 79–95.
Feng, Z., Fang, W., Li, Z., Wang, X., Huo, Q., Huang, C., Zhang, J., Zeng, H., 2011. Depositional environment of terrestrial petroleum source rocks and geochemical indicators in the Songliao Basin. Science China Earth Sciences 54, 1304–1317.
Flores, D., 2002. Organic facies and depositional palaeoenvironment of lignites from Rio Maior Basin (Portugal). International Journal of Coal Geology 48, 181–195.
Flores, D., Pereira, L.C.G., Ribeiro, J., Pina, B., Marques, M.M., Ribeiro, M.A., Bobos, I., de Jesus, A.P., 2010. The Buçaco Basin (Portugal): organic petrology and geochemistry study. International Journal of Coal Geology 81, 281–286.
Fowler, M., Hamblin, A., Hawkins, D., Stasiuk, L., Knight, I., 1995. Petroleum geochemistry and hydrocarbon potential of Cambrian and Ordovician rocks of western Newfoundland. Bulletin of Canadian Petroleum Geology 43, 187–213.
Ghienne, J.-F., 2003. Late Ordovician sedimentary environments, glacial cycles, and post-glacial transgression in the Taoudeni Basin, West Africa. Palaeogeography, Palaeoclimatology, Palaeoecology 189, 117–145.
Hasegawa, T., Pratt, L.M., Maeda, H., Shigeta, Y., Okamoto, T., Kase, T., Uemura, K., 2003. Upper Cretaceous stable carbon isotope stratigraphy of terrestrial organic matter from Sakhalin, Russian Far East: a proxy for the isotopic composition of paleoatmospheric CO2. Palaeogeography, Palaeoclimatology, Palaeoecology 189, 97–115.
Hemingway, J.D., Rothman, D.H., Grant, K.E., Rosengard, S.Z., Eglinton, T.I., Derry, L.A., Galy, V.V., 2019. Mineral protection regulates long-term global preservation of natural organic carbon. Nature 570, 228–231.
Huang, Y., Bond, D.P., Wang, Y., Wang, T., Yi, Z., Yuan, A., Jia, J., Su, Y., 2019. Early Triassic microbialites from the Changxing Region of Zhejiang Province, South China. Journal of Palaeogeography 8, 1–13.
Huang, Z., Li, Z., Zhu, Y., Shi, W., Li, Y., Li, Y., Huang, Y., Young, S., 2023. Organic matter accumulation of the Upper Triassic Ma'antang shales in the Longmenshan Foreland Basin (western Sichuan, China). Sedimentary Geology 444, 106318.
Ibach, L.E.J., 1982. Relationship between sedimentation rate and total organic carbon content in ancient marine sediments. AAPG Bulletin 66, 170–188.
Jenkyns, H.C., 2010. Geochemistry of oceanic anoxic events. Geochemistry, Geophysics, Geosystems 11, Q03004.
Jia, J., Liu, Z., Bechtel, A., Strobl, S.A., Sun, P., 2013. Tectonic and climate control of oil shale deposition in the Upper Cretaceous Qingshankou Formation (Songliao Basin, NE China). International Journal of Earth Sciences 102, 1717–1734.
Jones, B., Manning, D.A., 1994. Comparison of geochemical indices used for the interpretation of palaeoredox conditions in ancient mudstones. Chemical Geology 111, 111–129.
Kennedy, M.J., Pevear, D.R., Hill, R.J., 2002. Mineral surface control of organic carbon in black shale. Science 295, 657–660.
Khaled, A., Li, R., Xi, S., Zhao, B., Wu, X., Yu, Q., Zhang, Y., Li, D., 2022. Paleoenvironmental conditions and organic matter enrichment of the Late Paleoproterozoic Cuizhuang Formation dark shale in the Yuncheng Basin, North China. Journal of Petroleum Science and Engineering 208, 109627.
Kuypers, M.M., Blokker, P., Erbacher, J., Kinkel, H., Pancost, R.D., Schouten, S., Sinninghe Damsté, J.S., 2001. Massive expansion of marine archaea during a mid-Cretaceous oceanic anoxic event. Science 293, 92–95.
Lalonde, K., Mucci, A., Ouellet, A., Gelinas, Y., 2012. Preservation of organic matter in sediments promoted by iron. Nature 483, 198–200.
Li, Q., Wu, S., Xia, D., You, X., Zhang, H., Lu, H., 2020. Major and trace element geochemistry of the lacustrine organic-rich shales from the Upper Triassic Chang 7 Member in the southwestern Ordos Basin, China: implications for paleoenvironment and organic matter accumulation. Marine and Petroleum Geology 111, 852–867.
Li, L., Bao, Z., Li, Z., Chen, L., Xu, X., Li, Y., Zhao, Y., Song, X., 2024. Origin of quartz and its implications for different phase fluids in lacustrine shales from the Qingshankou Formation, southern Songliao Basin, China. Geoenergy Science and Engineering 234, 212673.
Liu, B., Schieber, J., Mastalerz, M., 2017. Combined SEM and reflected light petrography of organic matter in the New Albany Shale (Devonian–Mississippian) in the Illinois Basin: a perspective on organic pore development with thermal maturation. International Journal of Coal Geology 184, 57–72.
Liu, B., Bai, L., Chi, Y., Jia, R., Fu, X., Yang, L., 2019a. Geochemical characterization and quantitative evaluation of shale oil reservoir by two-dimensional nuclear magnetic resonance and quantitative grain fluorescence on extract: a case study from the Qingshankou Formation in Southern Songliao Basin, northeast China. Marine and Petroleum Geology 109, 561–573.
Liu, B., Wang, H., Fu, X., Bai, Y., Bai, L., Jia, M., He, B., 2019b. Lithofacies and depositional setting of a highly prospective lacustrine shale oil succession from the Upper Cretaceous Qingshankou Formation in the Gulong sag, northern Songliao Basin, northeast China. AAPG Bulletin 103, 405–432.
Liu, B., Teng, J., Mastalerz, M., Schieber, J., 2020. Assessing the thermal maturity of black shales using vitrinite reflectance: insights from Devonian black shales in the eastern United States. International Journal of Coal Geology 220, 103426.
Liu, B., Sun, J., Zhang, Y., He, J., Fu, X., Yang, L., Xing, J., Zhao, X., 2021. Reservoir space and enrichment model of shale oil in the first member of Cretaceous Qingshankou Formation in the Changling Sag, southern Songliao Basin, NE China. Petroleum Exploration and Development 48, 608–624.
Ma, L., Zhang, Y., Zhang, Z., Zhang, G., Wang, S., 2020. The geochemical characteristics of the Fengcheng Formation source rocks from the Halaalate area, Junggar Basin, China. Journal of Petroleum Science and Engineering 184, 106561.
MacLeod, K.G., Huber, B.T., Berrocoso, Á.J., Wendler, I., 2013. A stable and hot Turonian without glacial δ18O excursions is indicated by exquisitely preserved Tanzanian foraminifera. Geology 41, 1083–1086.
Martinez-Ruiz, F., Kastner, M., Gallego-Torres, D., Rodrigo-Gámiz, M., Nieto-Moreno, V., Ortega-Huertas, M., 2015. Paleoclimate and paleoceanography over the past 20,000 yr in the Mediterranean Sea Basins as indicated by sediment elemental proxies. Quaternary Science Reviews 107, 25–46.
Misch, D., Sachsenhofer, R., Bechtel, A., Gratzer, R., Groß, D., Makogon, V., 2015. Oil/gas–source rock correlations in the Dniepr-Donets Basin (Ukraine): new insights into the petroleum system. Marine and Petroleum Geology 67, 720–742.
Moldowan, J.M., Seifert, W.K., Gallegos, E.J., 1985. Relationship between petroleum composition and depositional environment of petroleum source rocks. AAPG Bulletin 69, 1255–1268.
Mulder, T., Alexander, J., 2001. The physical character of subaqueous sedimentary density flows and their deposits. Sedimentology 48, 269–299.
Mulder, T., Syvitski, J.P.M., Migeon, S., Faugères, J.-C., Savoye, B., 2003. Marine hyperpycnal flows: initiation, behavior and related deposits. A review. Marine and Petroleum Geology 20, 861–882.
Murray, J., Jagoutz, O., 2024. Clay minerals store organic carbon and cool Earth's climate over millions of years. Nature Geoscience 17, 8–9.
Neumeister, S., Misch, D., Algeo, T.J., Gawlick, H.-J., Gratzer, R., Sachsenhofer, R.F., 2020. Early diagenesis of organic-rich marls under shifting suboxic to euxinic conditions: the lower Toarcian of the Bächental basin. Marine and Petroleum Geology 120, 104513.
Owens, J.D., Lyons, T.W., Lowery, C.M., 2018. Quantifying the missing sink for global organic carbon burial during a Cretaceous oceanic anoxic event. Earth and Planetary Science Letters 499, 83–94.
Peters, K.E., 1986. Guidelines for evaluating petroleum source rock using programmed pyrolysis. AAPG Bulletin 70, 318–329.
Peters, K.E., Cassa, M.R., 1994. Applied source rock geochemistry. The Petroleum System: From Source to Trap. American Association of Petroleum Geologists, Tulsa.
Remírez, M.N., Algeo, T.J., 2020. Paleosalinity determination in ancient epicontinental seas: a case study of the T-OAE in the Cleveland Basin (UK). Earth-Science Reviews 201, 103072.
Rimmer, S.M., 2004. Geochemical paleoredox indicators in Devonian–Mississippian black shales, central Appalachian Basin (USA). Chemical Geology 206, 373–391.
Sageman, B.B., Meyers, S.R., Arthur, M.A., 2006. Orbital time scale and new C-isotope record for Cenomanian–Turonian boundary stratotype. Geology 34, 125–128.
Saggar, S., Parshotam, A., Sparling, G., Feltham, C., Hart, P., 1996. 14C-labelled ryegrass turnover and residence times in soils varying in clay content and mineralogy. Soil Biology and Biochemistry 28, 1677–1686.
Scaife, J., Ruhl, M., Dickson, A., Mather, T., Jenkyns, H., Percival, L., Hesselbo, S., Cartwright, J., Eldrett, J., Bergman, S., 2017. Sedimentary mercury enrichments as a marker for submarine large igneous province volcanism? Evidence from the Mid-Cenomanian event and Oceanic Anoxic Event 2 (Late Cretaceous). Geochemistry, Geophysics, Geosystems 18, 4253–4275.
Schouten, S., Hopmans, E.C., Forster, A., van Breugel, Y., Kuypers, M.M., Damsté, J.S.S., 2003. Extremely high sea-surface temperatures at low latitudes during the middle Cretaceous as revealed by archaeal membrane lipids. Geology 31, 1069–1072.
Song, Y., Liu, Z., Meng, Q., Xu, J., Sun, P., Cheng, L., Zheng, G., 2016. Multiple controlling factors of the enrichment of organic matter in the upper cretaceous oil shale sequences of the Songliao Basin, NE China: implications from geochemical analyses. Oil Shale 33, 142–166.
Tourtelot, H.A., 1979. Black shale—its deposition and diagenesis. Clays and Clay Minerals 27, 313–321.

Tribovillard, N., Algeo, T.J., Lyons, T., Riboulleau, A., 2006. Trace metals as paleoredox and paleoproductivity proxies: an update. Chemical Geology 232, 12–32.
Wang, C., Feng, Z., Zhang, L., Huang, Y., Cao, K., Wang, P., Zhao, B., 2013. Cretaceous paleogeography and paleoclimate and the setting of SKI borehole sites in Songliao Basin, northeast China. Palaeogeography, Palaeoclimatology, Palaeoecology 385, 17–30.
Wang, L., Tian, Y., Zhao, J., 2020. A rapid hydroclimate change and its influence on the Songliao Basin during the Santonian–Campanian transition as recorded by compound-specific isotopes. Palaeogeography, Palaeoclimatology, Palaeoecology 546, 109674.
Wei, W., Algeo, T.J., 2020. Elemental proxies for paleosalinity analysis of ancient shales and mudrocks. Geochimica et Cosmochimica Acta 287, 341–366.
Wignall, P.B., Twitchett, R.J., 1996. Oceanic anoxia and the end Permian mass extinction. Science 272, 1155–1158.
Wilkin, R., Barnes, H., Brantley, S., 1996. The size distribution of framboidal pyrite in modern sediments: an indicator of redox conditions. Geochimica et Cosmochimica Acta 60, 3897–3912.
Wu, Y., Tian, H., Li, T., Ji, S., Liu, Z., Xiao, X., Xie, L., 2021. Enhanced terrestrial organic matter burial in the marine shales of Yangtze platform during the early Carboniferous interglacial interval. Marine and Petroleum Geology 129, 105064.
Wu, Z., Littke, R., Baniasad, A., Yang, Z., Tang, Z., Grohmann, S., 2023. Geochemistry and petrology of petroleum source rocks in the Upper Cretaceous Qingshankou Formation, Songliao Basin, NE China. International Journal of Coal Geology 270, 104222.
Xi, D., Cao, W., Huang, Q., Do Carmo, D.A., Li, S., Jing, X., Tu, Y., Jia, J., Qu, H., Zhao, J., Wan, X., 2016. Late Cretaceous marine fossils and seawater incursion events in the Songliao Basin, NE China. Cretaceous Research 62, 172–182.
Xiao, H., Wang, T.-G., Li, M., Fu, J., Tang, Y., Shi, S., Yang, Z., Lu, X., 2018. Occurrence and distribution of unusual tri- and tetracyclic terpanes and their geochemical significance in some Paleogene oils from China. Energy & Fuels 32, 7393–7403.
Yandoka, B.M.S., Abdullah, W.H., Abubakar, M., Hakimi, M.H., Adegoke, A.K., 2015. Geochemical characterisation of Early Cretaceous lacustrine sediments of Bima Formation, Yola Sub-basin, Northern Benue Trough, NE Nigeria: organic matter input, preservation, paleoenvironment and palaeoclimatic conditions. Marine and Petroleum Geology 61, 82–94.
Yang, R., Jin, Z., van Loon, A.J., Han, Z., Fan, A., 2017. Climatic and tectonic controls of lacustrine hyperpycnite origination in the Late Triassic Ordos Basin, central China: implications for unconventional petroleum development. AAPG Bulletin 101, 95–117.
Zeng, S., Wang, J., Fu, X., Chen, W., Feng, X., Wang, D., Song, C., Wang, Z., 2015. Geochemical characteristics, redox conditions, and organic matter accumulation of marine oil shale from the Changliang Mountain area, northern Tibet, China. Marine and Petroleum Geology 64, 203–221.
Zhang, L., Bao, Z., Dou, L., Zang, D., Mao, S., Song, J., Zhao, J., Wang, Z., 2018. Sedimentary characteristics and pattern of distributary channels in shallow water deltaic red bed succession: a case from the Late Cretaceous Yaojia formation, southern Songliao Basin, NE China. Journal of Petroleum Science and Engineering 171, 1171–1190.
Zhang, P., Meng, Q., Misch, D., Sachsenhofer, R.F., Liu, Z., Hu, F., Shen, L., 2021. Oil shale potential of the Lower Cretaceous Jiufotang Formation, Beipiao Basin, Northeast China. International Journal of Coal Geology 236, 103640.
Zhang, P., Misch, D., Meng, Q., Sachsenhofer, R.F., Liu, Z., Jia, J., Gao, F., Bechtel, A., Hu, F., 2022. Lateral changes of organic matter preservation in the lacustrine Qingshankou Formation (Cretaceous Songliao Basin, NE China): evidence for basin segmentation. International Journal of Coal Geology 254, 103984.
Zhao, Z., Littke, R., Zieger, L., Hou, D., Froidl, F., 2020. Depositional environment, thermal maturity and shale oil potential of the Cretaceous Qingshankou Formation in the eastern Changling Sag, Songliao Basin, China: an integrated organic and inorganic geochemistry approach. International Journal of Coal Geology 232, 103621.
Zou, C., Yang, Z., Cui, J., Zhu, R., Hou, L., Tao, S., Yuan, X., Wu, S., Lin, S., Wang, L., 2013. Formation mechanism, geological characteristics and development strategy of nonmarine shale oil in China. Petroleum Exploration and Development 40, 15–27.
Zou, C., Feng, Y., Yang, Z., Jiang, W., Zhang, T., Zhang, H., Wang, X., Zhu, J., Wei, Q., 2023. Fine-grained gravity flow sedimentation and its influence on development of shale oil sweet sections in lacustrine basins in China. Petroleum Exploration and Development 50, 1013–1029.